Monthly Notices
of the
ROYAL ASTRONOMICAL SOCIETY

MNRAS **499,** 5891–5901 (2020)
Advance Access publication 2020 October 13

doi:10.1093/mnras/staa3135

AstroSat view of GRS 1915+105 during the soft state: detection of HFQPOs and estimation of mass and spin

H. Sreehari [1,2★] Anuj Nandi,[1★] Santabrata Das [3★] V. K. Agrawal,[1] Samir Mandal,[4] M. C. Ramadevi[1] and Tilak Katoch[5]

[1]*Space Astronomy Group, ISITE Campus, U. R. Rao Satellite Centre, Outer Ring Road, Marathahalli, Bangalore 560037, India*
[2]*Indian Institute of Astrophysics, Bangalore 560034, India*
[3]*Indian Institute of Technology Guwahati, Guwahati 781039, India*
[4]*Indian Institute of Space Science and Technology, Thiruvananthapuram 695547, India*
[5]*DAA, Tata Institute of Fundamental Research, Colaba, Mumbai 400005, India*

Accepted 2020 October 7. Received 2020 October 7; in original form 2020 April 1

ABSTRACT

We report the results of *AstroSat* observations of GRS 1915+105 obtained using 100 ks Guaranteed Time during the soft state. The colour–colour diagram indicates a variability class of δ with the detection of high-frequency quasi-periodic oscillation (HFQPO) in the power density spectra. The HFQPO is seen to vary in the frequency range of 67.96–70.62 Hz with percentage rms ∼0.83–1.90 per cent and significance varying from 1.63 to 7.75. The energy dependent power spectra show that the HFQPO features are dominant only in 6–25 keV energy band. The broad-band energy spectra (0.7–50 keV) of Soft X-ray Telescope and Large Area X-ray Proportional Counter modelled with `nthComp` and `powerlaw` imply that the source has an extended corona in addition to a compact 'Comptonizing corona' that produces high-energy emission and exhibits HFQPOs. The broad-band spectral modelling indicates that the source spectra are well described by thermal Comptonization with electron temperature (kT_e) of 2.07–2.43 keV and photon index (Γ_{nth}) between 1.73 and 2.45 with an additional `powerlaw` component of photon index (Γ_{PL}) between 2.94 and 3.28. The norm of `nthComp` component is high (∼8) during the presence of strong HFQPO and low (∼3) during the absence of HFQPO. Further, we model the energy spectra with the `kerrbb` model to estimate the accretion rate, mass, and spin of the source. Our findings indicate that the source accretes at super-Eddington rate of 1.17–1.31 $\dot{M}_{Edd}$. Moreover, we find the mass and spin of the source as 12.44–13.09 $M_\odot$ and 0.990–0.997 with 90 per cent confidence suggesting that GRS 1915+105 is a maximally rotating stellar mass X-ray binary black hole source.

Key words: accretion, accretion discs – black hole physics – X-rays: binaries.

1 INTRODUCTION

The astrophysical compact objects like white dwarf (WD), neutron star (NS), and black hole (BH) are often seen to exist along with its companion star. These binary sources are usually X-ray bright and referred as X-ray binaries (XRBs; Seward & Charles 2010). The high-energy X-ray emission from BH XRBs (BH-XRBs) is attributed to the accretion processes that are involved in the mass transfer from the companion star to the BH. Detailed study of the X-ray emission from BH-XRBs is essential to understand the accretion dynamics as well as the effect of strong gravity in the vicinity of the BHs.

XRBs are known to exhibit excess power in certain frequencies called quasi-periodic oscillations (QPOs) that are evident from the power density spectrum (PDS) of these sources (van der Klis et al. 1985; Belloni et al. 2005; Remillard & McClintock 2006; Nandi et al. 2012; Belloni & Motta 2016; Sreehari et al. 2019, and references therein). The QPOs in BH-XRBs lie in a wide range of frequencies ∼0.1–450 Hz and they have been classified into two general categories: (i) low-frequency QPOs (LFQPOs) in the range <40 Hz and (ii) high-frequency QPOs (HFQPOs) in the range ∼40–450 Hz (Remillard & McClintock 2006). The origin of HFQPOs is of great interest as these oscillations are transient as well as subtle. Moreover, HFQPOs possibly are the manifestations of various relativistic effects in the orbits close to the BH and it can be used as an important tool to probe general relativity in the strong gravity limit (Stella & Vietri 1998; Merloni et al. 1999; Rebusco 2008; Vincent et al. 2013; Stefanov 2014, and references therein). However, the conclusive consensus on the origin of HFQPOs is not reached yet.

Some BH-XRBs like GRS 1915+105 and IGR J17091−3624 also exhibit visually identifiable variabilities in their light curves. These variabilities are also associated with changes in the corresponding energy spectra and are categorized into several variability classes using colour–colour diagrams (CCDs), light-curve profiles (Belloni et al. 2000), and nature of energy spectra (Iyer, Nandi & Mandal 2015; Radhika et al. 2018).

Energy spectral modelling of various BH-XRBs indicates that the emission from these sources is in general thermal as well as non-thermal in nature. The multitemperature disc blackbody emission represents the Keplerian accretion disc (Shakura & Sunyaev 1973),

★ E-mail: hjsreehari@gmail.com (HS); anuj@ursc.gov.in (AN); sbdas@iitg.ac.in (SD)

whereas the high-energy emission from the source is attributed due to the inverse-Comptonization (Sunyaev & Titarchuk 1980; Chakrabarti & Titarchuk 1995; Tanaka & Lewin 1995) of seed photons by the hot corona located at the inner part of the disc surrounding the BH. Several other models along with the additional features like elemental abundance and relativistic-reflection (García et al. 2014, and references therein) have been introduced to explain overall emission features. However, these models are phenomenological in nature as they do not directly provide the physical properties (namely, mass and spin) of the accreting BH source. Keeping this in mind, in this paper we attempt to model the broad-band energy spectra of GRS 1915+105 using the `kerrbb` (Li et al. 2005) model. This model deals with rotating BH and is used to estimate the mass and spin of the sources.

Since detection, the source GRS 1915+105 has remained active in X-rays (Castro-Tirado, Brandt & Lund 1992). However, the source underwent into the non-active phase in the recent past although some flickering activities in X-rays were occasionally seen. It is noteworthy that GRS 1915+105 exhibits 14 different structured X-ray variability classes (Belloni et al. 2000; Klein-Wolt et al. 2002; Hannikainen et al. 2005). In a classical effort, Greiner, Cuby & McCaughrean (2001) estimated the mass of the source to be $M_{\rm BH} = 14 \pm 4$ M$_\odot$ considering the orbital period of ∼33.5 d. Recently, Reid et al. (2014) estimated the BH mass as $12.4^{+2.0}_{-1.8}$ M$_\odot$ and the distance as $8.6^{+2.0}_{-1.6}$ kpc using parallax method. Zdziarski (2014) calculated the inclination of GRS 1915+105 to be ∼65° based on kinematic constraints from the mass ejections. On the other hand, several attempts have been made to estimate the spin of the source. The estimation of spin of GRS 1915+105 is reported to be $a_{\rm k} = 0.98^{+0.01}_{-0.01}$ (Blum et al. 2009; Miller et al. 2013).

GRS 1915+105 exhibited LFQPOs during the *RXTE* era (Ratti, Belloni & Motta 2012, and references therein). Besides this, Yadav et al. (2016) detected LFQPOs from GRS 1915+105 using *AstroSat/LAXPC* data. GRS 1915+105 has also exhibited 67 and 40 Hz HFQPOs during the *RXTE* era (Morgan, Remillard & Greiner 1997; Strohmayer 2001b). Belloni et al. (2006) reported the detection of a 170 Hz HFQPO in the C-State of GRS 1915+105. Moreover, Belloni & Altamirano (2013) detected HFQPOs with frequencies varying from 63 to 71 Hz using *RXTE* data. Méndez et al. (2013) showed a detailed comparison of the lag spectra for 35 and 67 Hz HFQPOs of GRS 1915+105. Recently, Belloni et al. (2019) reported HFQPOs of frequencies between 67.4 and 72.3 Hz in the ω and μ variability classes of GRS 1915+105 from the *AstroSat* observations of 2016 July. They also studied the phase lags and their relation with hardness ratio, although they ignored the dead-time effect while carrying out power spectral analysis and detection of QPOs. Moreover, they did not carry out the broad-band spectral modelling to understand the emission processes. Meanwhile, several models were proposed to explain the origin of the HFQPOs observed in GRS 1915+105. Morgan et al. (1997) first proposed that the HFQPOs are associated with the Keplerian frequency at the innermost stable circular orbit (ISCO). Cui, Zhang & Chen (1998) suggested that the HFQPOs possibly arise due to the relativistic Lense–Thirring precession around a highly spinning BH. Nowak et al. (1997) proposed a model based on discoseismic g modes of oscillation for explaining the HFQPOs of this source. However, these models bear the limitations of revealing the inherent properties of the source under consideration including the relevant radiative emission processes.

Indeed, the broad-band X-ray spectra of GRS 1915+105 was studied (Grove et al. 1998; Zdziarski et al. 2001) with combined observations from *CGRO/OSSE* and *RXTE*. The spectra from few keV to 10 MeV showed a single *powerlaw* with no high-energy cut-off up to 500 keV, unlike other BH-XRBs. *RXTE* spectra of the source was modelled with just a thermal Comptonization component (Vilhu et al. 2001). *BeppoSAX* spectra of B and C states were found to have a definite high-energy cut-off, varying from 45 to 100 keV (Feroci et al. 1999).

Keeping all these in mind, in this paper we use Guaranteed Time (GT) *AstroSat* data of 2016 June to identify the variability class and characterize the detected HFQPOs of GRS 1915+105. We carry out the energy dependent study of power spectral features to understand the HFQPO properties. Combining the data from both imaging (Soft X-ray Telescope, *SXT*) and the proportional counter units (Large Area X-ray Proportional Counter, *LAXPC*) onboard *AstroSat*, we generate and fit the broad-band energy spectra with phenomenological as well as physical models in order to get an insight of the disc emission processes. Moreover, we attempt to constrain the mass and spin of the source using broad-band spectral modelling and finally compute the mass accretion rate as well.

We organize the paper as follows. In Section 2, we present the reduction and extraction procedures of *AstroSat* data. In Section 3, we discuss the methods of timing analysis and present the results. In Section 4, we carry out the spectral analysis and present the results of broad-band spectral modelling with *AstroSat* data. In Section 5, we attempt to constrain the mass and spin of the BH including the accretion rate. Finally, in Section 6 we discuss the results of our spectro-temporal studies of the BH source GRS 1915+105 and conclude.

2 OBSERVATION AND DATA REDUCTION

The source GRS 1915+105 was observed during the period of 2016 June 11 (MJD 57550) to 2016 June 15 (MJD 57554) using GT of *AstroSat* (Agrawal et al. 2017) for 100 ks (Observation ID: G05_189T01_9000000492). In this paper, we make use of the data from the imaging instrument *SXT* and the proportional counter *LAXPC* onboard *AstroSat*. *SXT* (Singh et al. 2017) operates in the 0.3–8 keV energy range. *LAXPC* (Antia et al. 2017) consists of three proportional counters (*LAXPC10, LAXPC20*, and *LAXPC30*) operating in the energy range of 3–80 keV with a high temporal resolution of 10 μs (Yadav et al. 2016).

SXT data reduction is carried out using the software provided by SXT-POC[1] at TIFR. Once the cleaned event files are generated using the pipeline, we use XSELECT tool to extract images, light curves, and spectra. However, as the *SXT* time resolution is poor (0.28 s), we do not use it for temporal analysis. For spectral modelling, we use the redistribution matrix files (rmfs), ancillary response files (arfs), and the background spectral files provided by the *SXT* instrument team at TIFR.[2]

We use the software available at the *AstroSat* science support cell[3] for the extraction of light curves of source as well as background from the *LAXPC* data. The response files and software for data extraction are provided by *LAXPC* instrument team of TIFR.[4] Further, we follow the procedures as described in Agrawal et al. (2018) and Sreehari et al. (2019) to extract energy spectra from both *SXT* and *LAXPC* observations. Once the light curves and energy spectra are generated, we carry out temporal and spectral modelling as detailed in Sections 3 and 4.

[1] http://www.tifr.res.in/~astrosat_sxt/sxtpipeline.html
[2] http://www.tifr.res.in/~astrosat_sxt/dataanalysis.html
[3] http://astrosat-ssc.iucaa.in/?q=data_and_analysis
[4] http://www.tifr.res.in/~astrosat_laxpc/LaxpcSoft.html

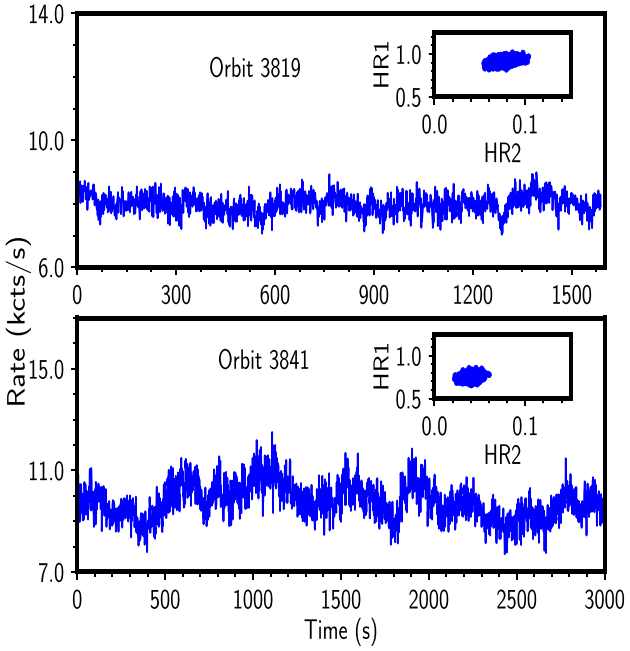

Figure 1. Dead-time corrected light curve in the energy range 3–60 keV for combined observations with *LAXPC10* and *LAXPC20*. The CCD is shown as inset of each panel. The top panel corresponds to the observation during Orbit 3819 where HFQPO is detected and the bottom panel corresponds to the observation during Orbit 3841, where HFQPO is absent. See text for details.

3 TIMING ANALYSIS AND RESULTS

We generate the light curves by combining data from *LAXPC10* and *LAXPC20* with 1 s binning for generating CCDs. CCDs are used to understand the hardness ratio variation and variability class of the source. Following this, we generate 1 ms binned light curves for generating the power spectra. The modelling of power spectra and the obtained results are presented in Section 3.2.

3.1 Colour–colour diagram

As mentioned before, we use light curves with 1 s binning for generating CCDs. The CCD depicts the variation of hardness ratios (HRs) such that $HR_1 = B/A$ and $HR_2 = C/A$, where A, B, and C are the count rates in 3–6, 6–15, and 15–60 keV energy bands, respectively. The background subtracted and dead-time corrected (see equation 1) light curves in the energy band 3–60 keV for the *LAXPC* observations on MJD 57551.04 (Orbit 3819) and MJD 57552.56 (Orbit 3841) are shown in Fig. 1. The background count rate is in the range of 100–140 counts s^{-1}. The CCDs are provided as inset in each panel which indicate that the maximum values of HR_1 and HR_2 for both the observations are less than 1.1 and 0.12, respectively. Comparing the CCDs and X-ray variability with *RXTE* observations (Belloni et al. 2000), we classify that the source is in its δ class during our observational campaign. However, both HR_1 and HR_2 values are seen to decrease as the source count rate increases whereas the reverse trend is observed towards the end (see Fig. 4 and Table 1). These findings indicate the signature of soft state (see Table 2 for spectral parameters). In addition, we do not find HFQPOs in those observations where mean values of $HR_1 \leq 0.76$ and $HR_2 \leq 0.04$ (see Table 1 and Section 3.2). In all the remaining observations, we detect HFQPOs.

3.2 Temporal properties

We generate power spectrum for each *LAXPC* observation considering a Nyquist frequency of 500 Hz in order to search for the presence of HFQPOs. We use intervals of 32 768 bins and compute the power spectrum for each interval, which is then averaged to obtain the final power spectrum. A geometric binning factor of 1.03 is used for representing the power spectrum in frequency space. After generating the Leahy power spectrum (Leahy et al. 1983), we carry out dead-time (τ_d) corrected Poisson noise subtraction following Agrawal et al. (2018) and Sreehari et al. (2019). Dead-time corresponds to the time interval between the successive photon detection by the detector. This effectively affects the Poisson noise level yielding the reduction of actual rms in the power spectrum. *LAXPC* has a dead-time of 42.5 μs (Yadav et al. 2016). Following van der Klis (1988), we calculate the incident count rate (r_{in}) as

$$r_{in} = \frac{r_{det}}{(1 - \tau_d\, r_{det}/N)}, \quad (1)$$

where r_{det} refers to the detected count rate and N is the number of proportional counter units used.

Thereafter, following Zhang et al. (1995, and references therein), we compute the dead-time affected Poisson noise power (P_n). Besides affecting the noise level, dead-time also modulates the source rms. So, after subtracting P_n level from the power spectrum, we correct for the dead-time effects on rms amplitude by scaling it using the relation given by

$$\mathrm{rms}_{in} = \mathrm{rms}_{det}\,(1 + \tau_d\, r_{in}/N) = \frac{\mathrm{rms}_{det}}{(1 - \tau_d\, r_{det}/N)}, \quad (2)$$

where rms_{in} is the dead-time corrected rms and rms_{det} is the rms detected by the instrument (see Bachetti et al. 2015; Sreehari et al. 2019, for details).

We model the PDS using a combination of *constant* and *Lorentzian* features, and illustrate it in frequency (Hz) versus rms^2/Hz plane. The *Lorentzian* has three parameters namely centroid frequency (ν), full width at half-maximum (FWHM), and normalization (norm). Here, a *Lorentzian* feature is adopted to define QPO, based on the values of its quality factor (Q = ν/FWHM), significance, and rms (see Sreehari et al. 2019, and references therein). The QPO rms is computed by finding the square root of the definite integral of the *Lorentzian* representing the QPO in frequency–power space. The QPO significance is computed as the ratio of *Lorentzian* normalization to its negative error (see Alam et al. 2014; Sreehari et al. 2019, and references therein).

Fig. 2 presents the PDS from combined *LAXPC10* and *LAXPC20* data corresponding to the Orbit 3860 in the frequency range from 0.06 to 500 Hz. The PDS is modelled with multiple `Lorentzians` and a `constant` that yields $\chi^2_{red} = 135.2/208 = 0.65$. Since the detected HFQPOs are seen to lie within a narrow range of frequencies, for the purpose of representation, we model the power spectra in the frequency range 20–200 Hz for all the observations.

Following the above consideration, we fit the PDS in the said frequency range (i.e. 20–200 Hz) with a *constant* and a *Lorentzian*. The modelled PDS for three *LAXPC* observations is shown in Fig. 3. The top panel (Orbit 3819) and the bottom panel (Orbit 3860) indicate detection of HFQPOs around 69 Hz. The middle panel representing the observation during Orbit 3841 does not indicate any HFQPO feature. Following Belloni, Méndez & Sánchez-Fernández (2001), we calculate the normalization of the `Lorentzian` feature in this observation (Orbit 3841) by freezing the `Lorentzian` centroid at 68.83 Hz and width at 1.4 Hz from the previous observation. The corresponding upper limit on significance is only 0.61. During our

Table 1. Details of HFQPO parameters from *LAXPC* observations of GRS 1915+105 in 3–25 keV energy band. These results are obtained from the observational data of *LAXPC10* and *LAXPC20* during δ class variability of the source. Errors corresponding to 68 per cent confidence are quoted for each parameter. See text for details.

MJD	Orbit	Exposure	$r_{\rm det}$ (cts s^{-1})	$r_{\rm in}$ (cts s^{-1})	QPO (Hz)	FWHM (Hz)	Significance (σ)	rms (per cent)	HR_1	HR_2	χ^2/dof
57550.97	3818	1982	6835	7996	$68.02^{+0.29}_{-0.24}$	$2.82^{+0.54}_{-0.64}$	7.75	1.90 ± 0.23	0.92	0.08	48/74
57551.04	3819	1590	6919	8112	$69.18^{+0.14}_{-0.27}$	1.49 fixed	6.94	1.56 ± 0.11	0.91	0.08	43/75
57551.12	3820	1030	6954	8159	$68.26^{+0.17}_{-0.28}$	$2.33^{+1.12}_{-1.11}$	3.45	1.46 ± 0.41	0.91	0.08	34/75
57551.19	3821	0791	7214	8520	$69.46^{+0.21}_{-0.15}$	$1.27^{+0.22}_{-0.21}$	4.17	1.18 ± 0.17	0.88	0.07	50/75
57551.25	3822	1215	7223	8533	$69.37^{+0.55}_{-0.70}$	$1.72^{+0.48}_{-0.42}$	3.19	0.98 ± 0.20	0.86	0.06	32/75
57551.33	3823	1638	7093	8352	$69.84^{+0.92}_{-0.36}$	1.72 fixed	2.06	0.89 ± 0.21	0.85	0.06	43/75
57551.40	3824	2063	7095	8355	$69.78^{+0.76}_{-0.26}$	$1.67^{+0.50}_{-0.41}$	2.16	1.00 ± 0.27	0.83	0.06	32/75
57551.47	3825	2516	7162	8448	$69.63^{+1.44}_{-0.34}$	$1.84^{+0.67}_{-0.53}$	2.94	0.86 ± 0.20	0.84	0.06	39/75
57551.53	3826	2941	7153	8435	$69.97^{+0.58}_{-0.32}$	$2.73^{+1.10}_{-0.88}$	3.86	1.12 ± 0.25	0.84	0.06	46/75
57551.61	3827	3364	7224	8534	$70.62^{+0.63}_{-0.93}$	$2.31^{+1.18}_{-1.08}$	4.26	0.85 ± 0.23	0.83	0.06	50/75
57551.84	3830	2953	7405	8787	$70.38^{+0.64}_{-1.01}$	$2.04^{+0.94}_{-1.00}$	3.84	0.83 ± 0.21	0.82	0.05	34/75
57552.35	3838	1116	7586	9045	$69.83^{+0.95}_{-0.27}$	1.18 fixed	1.63	0.91 ± 0.28	0.77	0.04	42/75
57552.41	3839	2180	7793	9339	$69.46^{+0.41}_{-0.35}$	1.46 fixed	2.49	0.83 ± 0.16	0.77	0.04	26/75
57552.47	3840	2603	8089	9768	$67.96^{+1.99}_{-1.84}$	$5.37^{+2.27}_{-1.85}$	2.95	1.01 ± 0.26	0.76	0.04	47/77
57552.56	3841	3027	8155	9865	–	–	–	–	0.75	0.04	39/77
57552.63	3843	2154	8076	9749	–	–	–	–	0.75	0.04	41/77
57552.86	3845	2402	7867	9446	–	–	–	–	0.76	0.04	38/77
57553.00	3848	1939	7738	9260	$69.96^{+1.08}_{-0.50}$	$2.57^{+2.32}_{-0.77}$	2.49	0.84 ± 0.35	0.77	0.04	36/75
57553.88	3860	2381	6813	7966	$69.22^{+0.17}_{-0.24}$	$2.53^{+1.18}_{-1.63}$	3.74	1.42 ± 0.44	0.88	0.07	45/75
57553.95	3862	2042	6918	8110	$68.98^{+0.33}_{-0.43}$	$3.78^{+1.15}_{-1.12}$	5.36	1.45 ± 0.25	0.88	0.07	34/75
57554.02	3863	1755	6965	8176	$69.03^{+0.29}_{-0.41}$	$3.35^{+1.04}_{-1.23}$	5.23	1.50 ± 0.29	0.88	0.07	38/75
57554.09	3864	1170	6888	8070	$69.20^{+0.15}_{-0.14}$	$2.00^{+0.27}_{-0.26}$	7.43	1.49 ± 0.14	0.89	0.07	41/75
57554.16	3865	1156	6638	7728	$69.01^{+0.24}_{-0.33}$	$2.55^{+0.87}_{-1.33}$	4.61	1.63 ± 0.39	0.90	0.08	36/75

Table 2. Broad-band spectral modelling parameters from the model `Tbabs(nthComp + powerlaw)`. Observations in which HFQPOs are absent are tabulated separately. Errors are computed with 90 per cent confidence.

MJD (Orbit)	$kT_{\rm bb}$ (keV)	$kT_{\rm e}$ (keV)	$\Gamma_{\rm nth}$	$\rm norm_{nth}$	$\Gamma_{\rm PL}$	$\rm norm_{PL}$	Flux (erg cm^{-2} s^{-1})	χ^2/dof
Detection of HFQPOs								
57551.33 (3823)	0.3	2.25 ± 0.08	1.79 ± 0.07	8.1	2.94 ± 0.12	15.8	3.09×10^{-8}	440/415 = 1.06
57551.53 (3826)	0.19 ± 0.02	2.32 ± 0.03	1.76 ± 0.01	8.6	3.04 ± 0.01	17.6	3.11×10^{-8}	655/551 = 1.18
57551.84 (3830)	0.1	2.23 ± 0.02	1.73 ± 0.03	8.9	3.04 ± 0.04	15.5	3.22×10^{-8}	737/628 = 1.17
57552.41 (3839)[a]	0.1	2.07 ± 0.18	2.24 ± 0.86	3.9	3.28 ± 0.03	34.9	3.34×10^{-8}	441/339 = 1.30
57553.88 (3860)	0.1	2.43 ± 0.13	1.74 ± 0.06	7.0	3.09 ± 0.04	25.5	3.07×10^{-8}	615/547 = 1.12
Non-detection of HFQPOs								
57552.56 (3841)	0.1	2.09 ± 0.15	2.45 ± 0.84	3.01	3.28 ± 0.02	30	3.55×10^{-8}	729/636 = 1.14

Note. [a]Weakest HFQPO.

AstroSat campaign, 18 more such HFQPO signatures are detected having frequencies in the range of 67.96–70.62 Hz. The model fitted parameters of these HFQPOs like centroid frequency, FWHM, significance, and rms along with the HR variations are presented in Table 1. These detections are consistent with the *RXTE* observation of variable HFQPOs (63.5–71.3 Hz), with an average of 67.3 ± 2.0 Hz (Morgan et al. 1997; Belloni & Altamirano 2013).

In Fig. 4 (left), we present the time evolution of the source count rate (top panel), HFQPO frequency (middle panel), and QPO rms (bottom panel). The variation of count rate within the soft state spanned over a few days is also to be noted. In the top panel, the red stars indicate the observations in which HFQPOs are absent. In the middle and bottom panels, all the HFQPO detections are presented and the blue stars indicate the HFQPOs with significance above 3. Fig. 4 (right) shows the correlation of QPO frequency and QPO rms with count rate. It is evident that as the source count rate increases and HR value decreases (see Table 1), the HFQPO rms reduces and eventually disappears. The vertical green bars indicate the observations during Orbits 3819, 3841, and 3860 that we present in Fig. 3. From Table 1, we find that the percentage rms of HFQPO lies in the range of 0.83 per cent to 1.90 per cent. The dead-time correction factor for rms is obtained in the range 1.17–1.21. The HFQPO is weak or below the significance level of detection, when the source count rate peaks.

The $\chi^2_{\rm red}$ values for power spectral modelling are provided in Table 1. Modelling the PDS (Orbit 3860) in the frequency range 20–200 Hz with only a constant yields a $\chi^2_{\rm red}$ of 97.68/78 = 1.25. However, the presence of excess power above the constant level

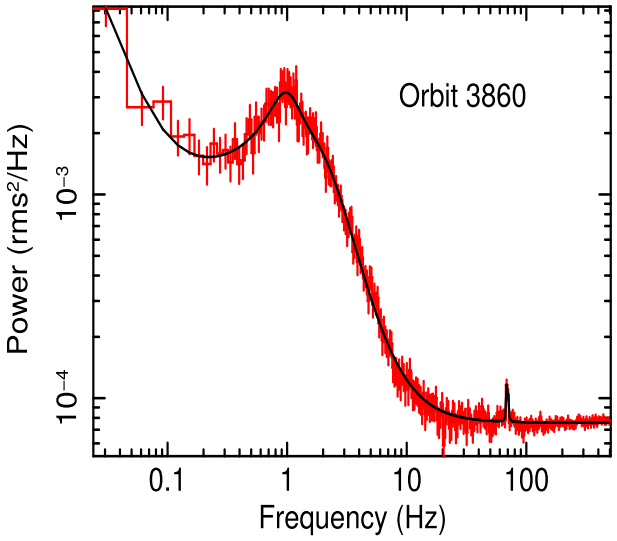

Figure 2. Power spectrum for the observation of Orbit 3860 from combined *LAXPC10* and *LAXPC20* data in the broad frequency range from 0.06 to 500 Hz. PDS is modelled with multiple `Lorentzians` and a `constant` component.

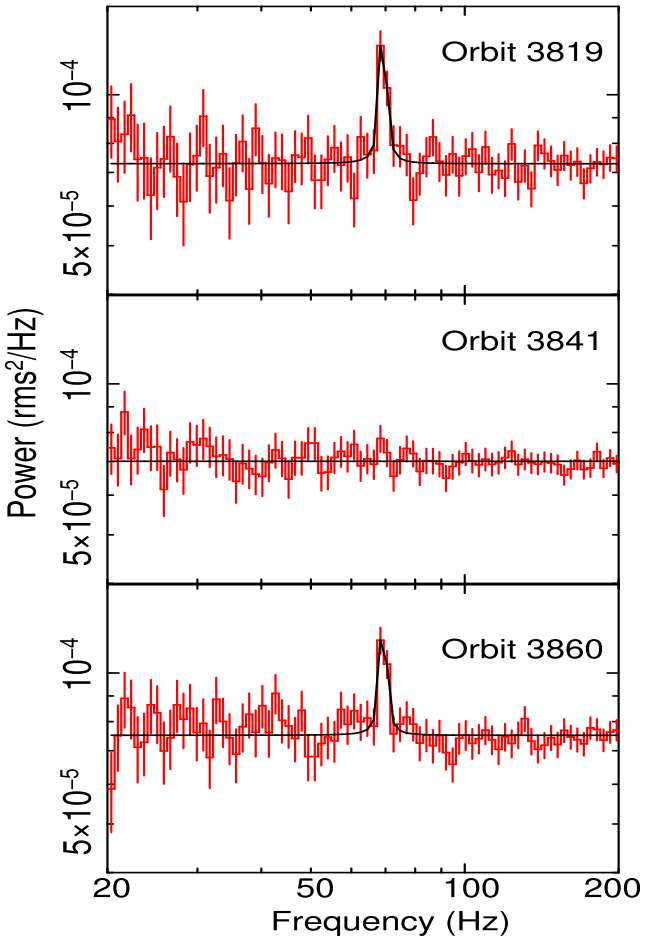

Figure 3. Combined power spectra of *LAXPC10* and *LAXPC20* in 3–25 keV energy band, for three orbits of *AstroSat* observations. HFQPOs are detected during Orbits 3819 and 3860, whereas no such detection is seen during Orbit 3841 (middle panel). See text for details.

around 69 Hz indicates the presence of a QPO. This feature is further modelled with a `Lorentzian` apart from the constant resulting in an overall $\chi^2_{\rm red}$ of 45/75 = 0.6. The decrease of $\chi^2_{\rm red}$ from 1.25 to 0.6 suggests that HFQPO feature is significant and requires modelling. Moreover, we detect the `Lorentzian` feature at 69 Hz in several observations which indicates that it is not a random increase in amplitude and hence we argue that it is not a case of overfitting.

Since HFQPOs are detected in several observations, we intend to carry out energy dependent behaviour of these oscillations. For this purpose, we generate PDS from light curves in the energy range of 3–6, 6–25, and 25–60 keV and model them in the frequency range of 20–200 Hz. Fig. 5 shows the energy dependent PDS for MJD 57551.04 (Orbit 3819). It is evident that the HFQPO is present only in the 6–25 keV energy band (middle panel) and not in the lower (3–6 keV) and higher (25–60 keV) energy bands. We find that the upper limit of the significance in the energy range 3–6 and 25–60 keV are 1.69 and 0.44, respectively. The strong HFQPO feature (Q-factor $\sim$ 46, significance of 6.45σ, and rms of 2.15 $\pm$ 0.23 per cent) in the 6–25 keV energy band is found at $68.75^{+0.12}_{-0.12}$ Hz. All *LAXPC* observations of GRS 1915+105 have similar power spectral features (non-detection of HFQPO signals) in the 3–6 and 25–60 keV band. However, the HFQPO strength (rms) and significance varies over the observations as can be seen from Table 1. The absence of HFQPO feature in 3–6 keV energy band indicates that the QPOs are likely to be the result of an oscillating corona located in the vicinity of the BH and it emits in 6–25 keV energy band. In order to have better clarity on the energy dependence of HFQPOs and understand the emission processes, we carry out the broad-band energy spectral modelling of *AstroSat* data of GRS 1915+105 and present the results in Section 4.

4 SPECTRAL ANALYSIS AND RESULTS

To carry out the spectral analysis, we use simultaneous data from both *SXT* and *LAXPC*. The latest calibration files are provided by *AstroSat* mission team.[5] A systematic of 2 per cent is added per spectral bin as suggested by Antia et al. (2017) and Leahy & Chen (2019).

SXT spectra are extracted in the 0.7–7 keV band, whereas dead-time corrected *LAXPC* spectra (Antia et al. 2017) are extracted in the energy range of 3–50 keV (see Agrawal et al. 2018; Sreehari et al. 2019, for details). As there are only a few good quality data available from *SXT* in the data base,[6] we are able to generate broad-band spectra only for those observations. Modelling of the *SXT* spectra indicates an nH column density (in 10^{22} atoms cm^{-2}) in the range 5.93 $\pm$ 1.01 to 6.07 $\pm$ 1.19. We model the energy spectra with fixed nH of 6 $\times$ 10^{22} atoms cm^{-2} and the obtained spectral parameters are quoted in Table 2. The change in parameters due to the variation of nH is within the error bars of the values obtained by freezing nH at 6 $\times$ 10^{22} atoms cm^{-2}. Gain correction is applied using `gain fit` routine of XSPEC on all the *SXT* spectra to account for the instrumental feature peaks at 1.8 and 2.2 keV. Initially, we model the broad-band spectra with phenomenological model combination `Tbabs(diskbb + powerlaw × smedge)` that yields a disc temperature of 2.57 $\pm$ 0.05 keV, photon index of 3.11 $\pm$ 0.06 for the observation on MJD 57551.33 (Orbit 3823) with a χ^2/dof = 438/418 = 1.04. Using `cflux` model, we estimate the disc contribution that is found to be 69.7 per cent of the total flux. This indicates that the source is in thermally dominated soft state. This

[5] http://astrosat-ssc.iucaa.in/?q=laxpcData
[6] https://astrobrowse.issdc.gov.in/astro_archive/archive/Home.jsp

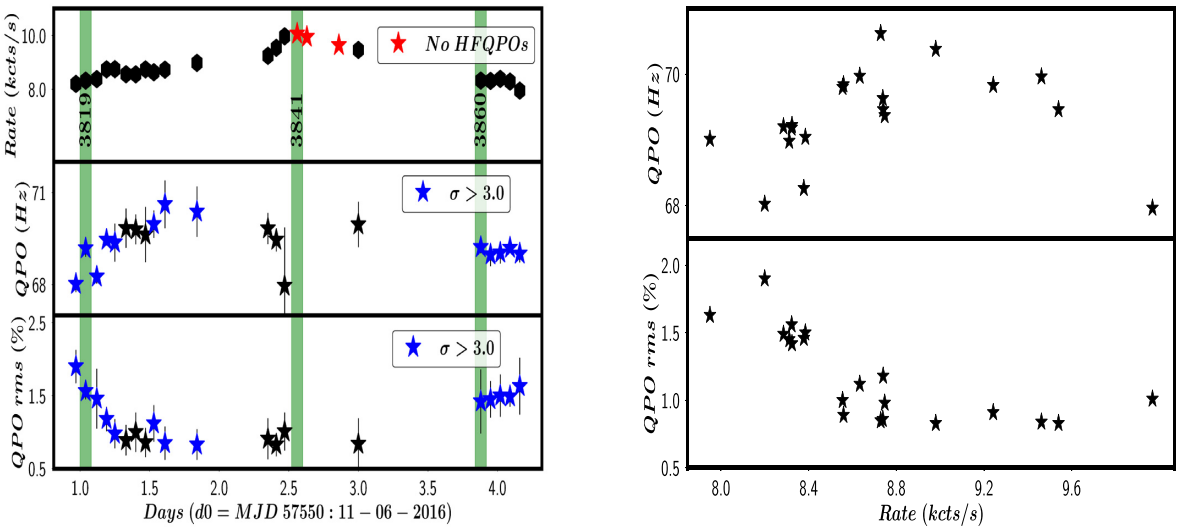

Figure 4. LHS: Top panel depicts the dead-time corrected source count rate for each observation. The red asterisks indicate observations where HFQPO is absent. The middle panel shows the frequency of all detected HFQPOs and the ones above 3σ significance are presented in blue colour. The bottom panel shows the corresponding HFQPO rms. The vertical green shades represent the observations for which the power spectra are presented in Fig. 3. RHS: The variation of QPO frequency with count rate is shown in the top panel and the dependence of QPO rms on count rate is presented in the bottom panel.

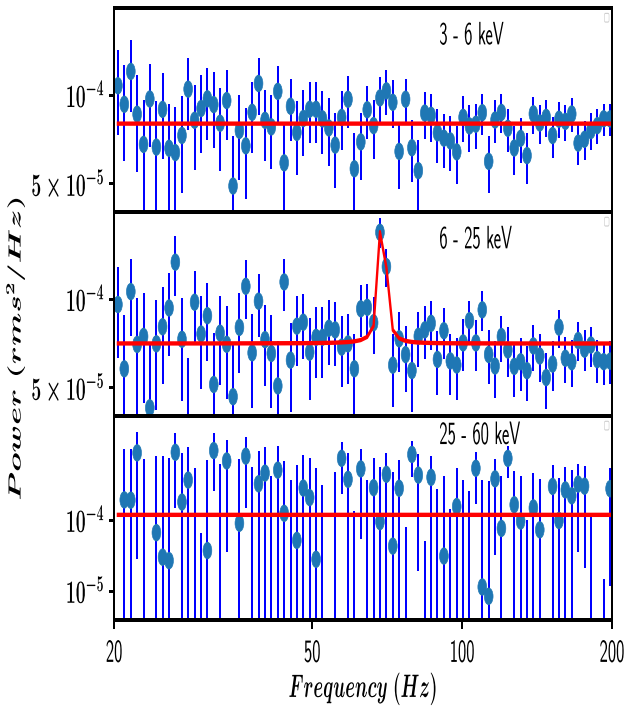

Figure 5. The energy dependent power spectra for the observation corresponding to Orbit 3819 are shown. Top panel indicates that there is no signature of QPO in the 3–6 keV energy band. The middle panel corresponding to 6–25 keV energy band shows significant detection of HFQPO. Bottom panel is for 25–60 keV energy band where power spectrum is noise dominated without any detection of QPO. See text for details.

also corroborates the CCDs representing the light curve (i.e. δ class) as a softer state of GRS 1915+105.

In order to understand the physical processes leading to the emission from the source, we fit the broad-band energy spectrum of Orbit 3823 with the thermal Comptonization model (`nthComp` in XSPEC; Zdziarski, Johnson & Magdziarz 1996). The fit resulted with $\chi^2_{\rm red} = \chi^2/{\rm dof} = 1534/420 = 3.65$ as the higher energy part of the spectrum (above 30 keV) is not fitted with `nthComp` model. Upon inclusion of an additional power-law component, the combined models provide acceptable fit with $\chi^2_{\rm red} = \chi^2/{\rm dof} = 440/415 = 1.06$. Hereafter, we carry out the broad-band spectral modelling with the combined models defined as `Tbabs(nthComp + powerlaw)`. The model parameters of `nthComp` are electron temperature ($kT_{\rm e}$) equal to 2.25 ± 0.08 keV, seed-photon temperature ($kT_{\rm bb}$) of ∼0.30 keV, and photon index ($\Gamma_{\rm nth}$) of 1.79 ± 0.07. An additional `powerlaw` component with a photon index ($\Gamma_{\rm PL}$) of 2.94 ± 0.12 is required to fit the high-energy part of the spectrum (above ∼25 keV). Following this approach, we model the broad-band spectral data for all the available observations irrespective of the presence of HFQPOs (see Table 2).

In the left-hand panel of Fig. 6, we depict the unfolded spectrum of an observation (MJD 57552.56, Orbit 3841) for which HFQPO feature is not seen in the PDS (middle panel of Fig. 3). The fitted parameters are obtained as $kT_{\rm e} \sim 2.09$ keV and $\Gamma_{\rm nth} = 2.45 \pm 0.84$, respectively. The `powerlaw` index in this case is obtained as $\Gamma_{\rm PL} \sim 3.28$. Further, we model the broad-band energy spectrum for the observation on MJD 57553.88 (Orbit 3860) that shows a significant (3.74σ) detection of HFQPO in the PDS (bottom panel of Fig. 3). In the right-hand panel of Fig. 6, we present the unfolded spectrum modelled with `Tbabs(nthComp × smedge + powerlaw)`. The `nthComp` component yields $\Gamma_{\rm nth} = 1.74 \pm 0.06$ and $kT_{\rm e} \sim 2.43$ keV. The `powerlaw` component is seen to be strong with a steep photon index of $\Gamma_{\rm PL} = 3.09 \pm 0.04$. The additional `smedge` component that is not required for Orbit 3841 is, however, used to model the absorption feature around 7 keV. The model fitted parameters for all the broad-band observations are presented in Table 2. It may also be noted that the energy spectral parameters for orbit 3839, which has the detection of the weakest HFQPO (rms ∼0.83 per cent and significance ∼2.49) corresponds to a weak `nthComp` ($\rm norm_{nth} \sim 3.9$) and a strong `powerlaw` ($\rm norm_{PL} \sim 34.9$) contribution. We discuss the implications of these results in Section 6.

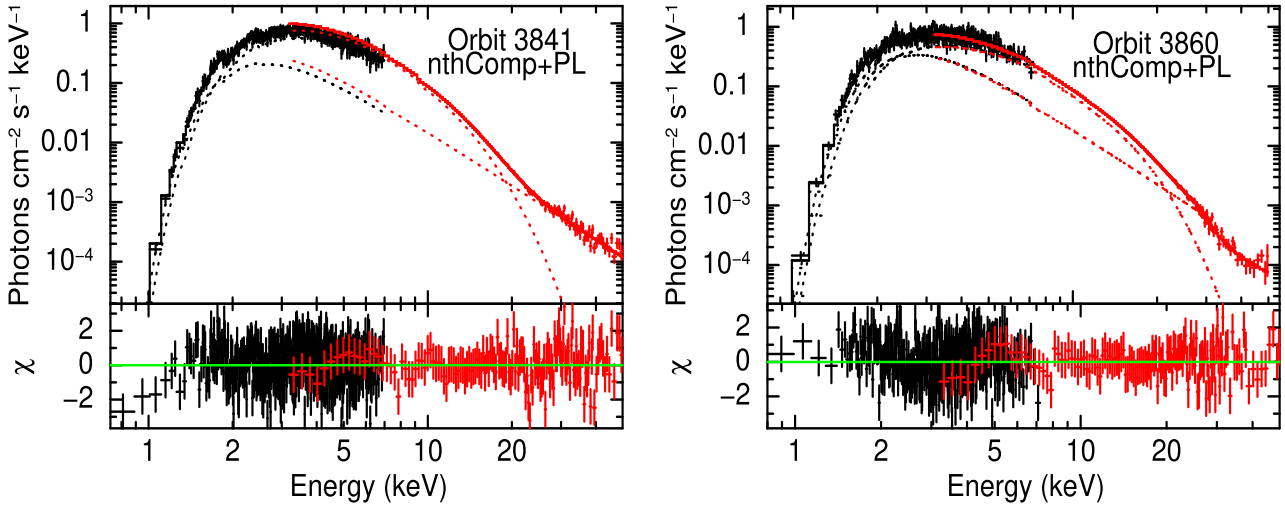

Figure 6. The best-fitting unfolded energy spectra (0.7–50 keV) of GRS 1915+105 observed on MJD 57552.56 (Orbit 3841) and MJD 57553.88 (Orbit 3860) with *AstroSat*. The spectra are modelled with `Tbabs(nthComp + powerlaw)`. The bottom panel of each spectrum shows residuals in units of σ. See text for details.

Table 3. Broad-band spectral modelling parameters from `Tbabs(simpl * kerbb × smedge)constant`. Errors are computed with 90 per cent confidence.

MJD (Orbit)	Γ	Frac. scattered (F_{sca})	$\dot{M}$ (10^{18} g s^{-1})	Mass ($M_\odot$)	a_k	E_{smedge} (keV)	χ^2/dof
57551.53 (3826)	3.92 ± 0.01	0.13 ± 0.01	7.65 ± 0.11	12.66 ± 0.22	0.996 ± 0.001	6.41 ± 0.42	(657/564=1.16)
57551.84 (3830)	3.83 ± 0.01	0.09 ± 0.01	7.73 ± 0.07	12.75 ± 0.16	0.996 ± 0.001	6.44 ± 0.40	(733/629=1.16)
57552.56 (3841)	3.09 ± 0.01	0.05 ± 0.01	7.89 ± 0.07	12.92 ± 0.17	0.991 ± 0.001	7.88 ± 0.86	(717/639=1.12)
57553.88 (3860)	4.80 ± 0.01	0.55 ± 0.01	7.05 ± 0.10	12.85 ± 0.24	0.995 ± 0.001	5.08 ± 0.70	(662/559=1.18)

5 ESTIMATION OF MASS, SPIN, AND ACCRETION RATE

In this section, we present the results of broad-band spectral modelling (Orbits 3826, 3830, 3841, 3860) to constrain the mass and spin of the source. While doing this, we use the `kerrbb` model (Li et al. 2005) along with the `simpl` model (Steiner et al. 2009) of XSPEC (Arnaud 1996) to fit the spectra. The `kerrbb` model represents a thin, general relativistic multitemperature blackbody disc around a rotating BH whereas the `simpl` is a Comptonization model in which a fraction of the seed photons is scattered into a power-law distribution. Following the spectral analysis method discussed in the previous section, we model the broad-band observations with a combination of models as `Tbabs(simpl * kerbb × smedge)constant` that results into acceptable fit with $\chi^2_{red} \sim 1$ (see Table 3). The model fitted energy spectra for Orbits 3841 and 3860 are shown in Fig. 7. We find that the model fitted parameters of BH mass $M_{BH} = 12.92 \pm 0.17$ M$_\odot$, accretion rate $\dot{M} \sim 7.89 \times 10^{18}$ g s^{-1}, and spin $a_k = 0.991 \pm 0.001$ for the observation of Orbit 3841. Similarly, we obtain $M_{BH} = 12.85 \pm 0.24$ M$_\odot$, $\dot{M} \sim 7.05 \times 10^{18}$ g s^{-1}, and $a_k = 0.995 \pm 0.001$ for the observation of Orbit 3860. Interestingly, the accretion rate corresponding to non-detection of HFQPO (Orbit 3841) is higher than that in observations where HFQPO is detected. It is to be noted that two additional `Gaussians` are used at 1.8 and 2.2 keV to account for the instrumental peaks at these energies, instead of using `gain fit`.

In Table 3, we present the spectral fit parameters for all broad-band observations, where columns 1–8 represent observation date with Orbit number, photon index (Γ), scattered fraction (F_{sca}), accretion rate ($\dot{M}$), BH mass (M_{BH}) in solar mass unit (M$_\odot$), spin (a_k), `smedge` energy (E_{smedge}), and χ^2_{red} (χ^2/dof), respectively. The index (Γ) varies from 3.08 to 4.80, whereas scattered fraction of seed photons is minimum ($F_{sca} \sim 0.05$) when the HFQPO is absent and maximum ($F_{sca} \sim 0.55$) when the HFQPO signal is most significant. Adopting the source mass as obtained from the spectral fitting (see Table 3), and considering the source distance as ∼8.6 kpc (Reid et al. 2014), we find that GRS 1915+105 accretes at super-Eddington rate of 1.17–1.31 $\dot{M}_{Edd}$ during the GT phase *AstroSat* observations under consideration.

Further, we examine the dependence of accretion rate and spin on the mass of the source. Fig. 8 (left) shows the confidence contours obtained for mass of the BH and the accretion rate for the Orbit 3860. Similarly, in Fig. 8 (right) we depict the confidence contours of mass and spin of the source for the same observation. It indicates that the BH mass (M_{BH}) lies in the range 12.85 ± 0.24 M$_\odot$ and spin (a_k) lies in the range 0.993–0.996. The red, green, and blue curves represent contours of 68 per cent, 90 per cent, and 99 per cent confidence, respectively.

Since our goal is to estimate BH parameters, we have also attempted with the `kerrd` model (Ebisawa et al. 2003). The spectral fits yield a mass range of 11.66–12.69 M$_\odot$ and accretion rate of 7.05–7.75 ($\times 10^{18}$ g s^{-1}). The mass estimate from `kerrd` model is marginally lower than the estimates from `kerrbb`, while the accretion rate estimate from both models is consistent. It may be noted that `kerrd` model assumes fixed spin value as 0.998, whereas the spin is treated as free parameter in `kerrbb` model, besides accretion rate and mass. Because of that we prefer `kerrbb` model over `kerrd` model and quote the parameters from `kerrbb` model as our final result.

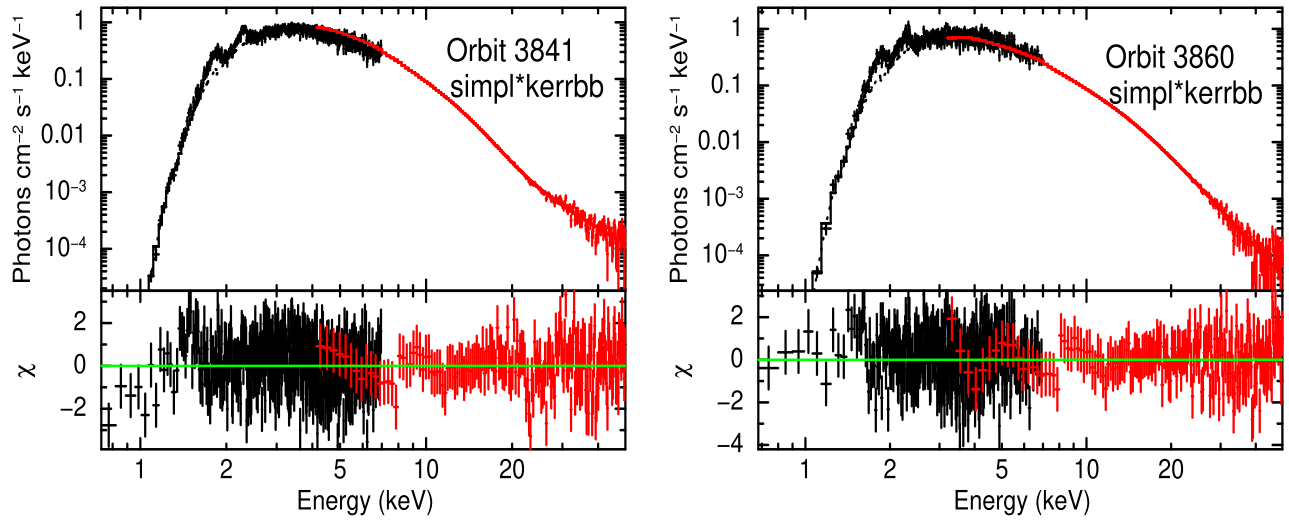

Figure 7. The best-fitting unfolded energy spectra (0.7–50 keV) of GRS 1915+105 observed on MJD 57552.56 (Orbit 3841) and MJD 57553.88 (Orbit 3860) with *AstroSat*. The spectra are modelled with `Tbabs(simpl*kerrbb × smedge)constant`. The bottom panel of each figure shows residuals in units of σ.

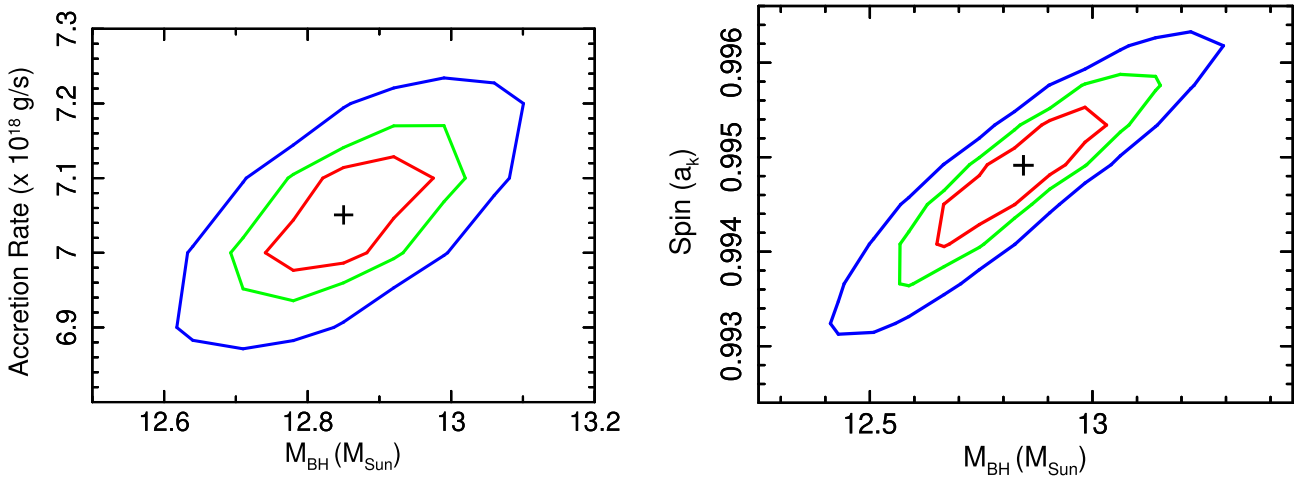

Figure 8. The confidence contours of two parameters namely accretion rate ($\dot{M}$) and mass of the BH ($M_{\rm BH}$) for the observation during Orbit 3860 is shown on the left-hand panel. On the right-hand panel, we show the confidence contours for the mass ($M_{\rm BH}$) and spin ($a_{\rm k}$). The red, green, and blue contours show delta fit statistic of 2.30 (68 per cent), 4.61 (90 per cent), and 9.21 (99 per cent), respectively.

6 DISCUSSION AND CONCLUSION

In this paper, we study the spectro-temporal properties of GRS 1915+105 using GT phase observations of the *AstroSat* data. The CCDs indicate that the source exhibits δ class variability (Belloni et al. 2000) with small hardness ratios ($HR_1 < 1.1$, $HR_2 < 0.12$). During our observational campaign, GRS 1915+105 was in the soft state and significant variations in the count rate (7728–9865 cts s^{-1}), HR1 (0.75–0.92), and HR2 (0.04–0.08) are observed. We also find that HFQPOs disappear at high count rates and the disc fraction varies from 51 per cent to 69.7 per cent. This result indicates that the source presumably was in a time varying soft state during our campaign.

We detect HFQPOs at ∼69 Hz from the source during *AstroSat* observations. It is observed that the strength of the HFQPOs decreases and eventually disappears as the source count rate increases (see Fig. 4) and hardness ratios decreases (see Fig. 1 and Table 1). However, we have not observed significant change in the QPO frequency as the count rate varies. The dependence of QPO parameters on source intensity has been studied earlier by van der Klis et al. (1985), where they found a significant increase in frequency and decrease in strength of QPOs with increasing count rates. Cui (2000) found that HFQPOs disappear with an increase in accretion rate in Low Mass X-ray Binary (LMXB) systems, which is also seen in our analysis. On the other hand, the disappearance of LFQPOs in LMXBs is shown to be associated with radio flares (Fender, Homan & Belloni 2009; Nandi, Radhika & Seetha 2013; Radhika & Nandi 2014) and is followed by the subsequent softening of the energy spectra (Radhika et al. 2016). During our observations, the hardness ratios of the source (see Table 1) also indicate that the source becomes relatively softer when the HFQPOs are absent. From the energy dependent power spectra, it is evident that the HFQPOs are present only in the 6–25 keV (see Fig. 5) but not in the 3–6 and 25–60 keV energy bands. Following Belloni et al. (2001), we calculate the upper limit of the QPO significance in 3–6 keV as 1.69 and in 25–60 keV as 0.44. The rms amplitude of the HFQPOs in our observations is found to vary within 0.83–1.90 per cent and the frequencies of these HFQPOs lie in the range of 67.96–70.62 Hz. Belloni & Altamirano (2013) also

reported HFQPO of frequency 67.4 ± 2.0 Hz, using RXTE data of the same source. Recently, Belloni et al. (2019) reported a variable HFQPO in the range between 67.4 and 72.3 Hz, where higher phase lags are observed in harder regions.

HFQPOs are detected in other BH-XRB sources, such as GRO J1655−40, XTE J1550−564, and H 1743−322 (Remillard & McClintock 2006). Phase-lag studies of the 67 Hz QPO in GRS 1915+105 (Cui 1999; Méndez et al. 2013) indicates that the hard photons lag the soft photons. This is consistent with our scenario where soft radiation from the accretion disc is inverse-Comptonized within a compact corona around the BH. A 66 Hz HFQPO was detected in the BH binary source IGR J17091−3624 by Altamirano & Belloni (2012). They have discussed the possibility that this HFQPO (∼67 Hz) detected in both GRS 1915+105 and IGR J17091−3624 is linked to the physical processes that produce low-frequency structured variability exhibited by these two sources.

Several models have been proposed to explain the origin of these QPOs. The relativistic precession model by Stella & Vietri (1998) considers that HFQPOs are associated with the orbital frequency as well as the nodal and the periastron precession frequencies. Rezzolla et al. (2003) proposed a model where HFQPOs are attributed to the pressure mode oscillations of an accretion torus orbiting the BH. Recently, in a theoretical attempt, Dihingia et al. (2019) showed that shock induced accretion solutions around a rapidly rotating stellar mass BH are viable to account for such an HFQPO phenomenon. Interestingly, Varniere, Vincent & Casse (2020) explored the possibility of HFQPO generation resulting from vortices formed due to Rossby wave instability at the inner edge of the accretion disc. As the centroid frequencies of the HFQPOs do not vary beyond a few per cent, we conjecture that it perhaps originated from the vicinity of the source and therefore carries the imprint of the effect of strong gravity, namely the mass and spin of the BH.

In order to explain the radiative properties of the accretion flow around the source, we carry out the broad-band energy spectral modelling using combined *SXT* and *LAXPC* data in the 0.7–50 keV energy range. Modelling of spectra with a multitemperature disc blackbody (diskbb) along with a powerlaw indicates high disc contribution (51–69.7 per cent) to the total emitted radiative flux. We find relatively steeper photon index (∼3) and high disc temperature (∼2.5 keV) that eventually indicate the source belongs to the soft state.

Next, to examine the physical processes and the spectral parameters, we model the spectra using nthComp and powerlaw. The photon index ($\Gamma_{\rm nth}$) is seen to be small and remain nearly constant ($\Gamma_{\rm nth} \sim 1.7$) during the HFQPO observations whereas $\Gamma_{\rm nth}$ becomes large ($\Gamma_{\rm nth} \sim 2.45$) when HFQPO is not detected (see Table 2). It may be noted that the seed photon temperature does not change appreciably ($kT_{\rm bb} \sim 0.1$–0.3 keV) in these observations. We find electron temperature $kT_{\rm e}$ in the range 2.07–2.43 keV (i.e. an exponential roll over energy ∼7.3 keV) and $1.73 < \Gamma_{\rm nth} < 2.45$ for broad-band spectra. In addition, an extended corona seems to be present as well, because an additional powerlaw component with higher photon index ($\Gamma_{\rm PL} \sim 3$) is required to model the higher energy part of the spectrum (above 25 keV). Indeed, it may be plausible that the accretion flow harbours a cool and compact central corona that not only exhibits HFQPOs, but also emits high-energy photons till ∼25 keV (see Figs 5 and 6). Also, surrounding the inner compact corona, a diffuse but relatively hot extended 'Compton' corona may be present which is likely to produce hard X-ray photons up to ∼50 keV. The existence of such an extended coronal structure around GRS 1915+105 would be possible as the source may not swallow all the matter accreted at super-Eddington rate (Done, Wardziński & Gierliński 2004; Punsly & Rodriguez 2013).

The broad-band spectra of observations with relatively higher rms of HFQPOs indicate a weaker extended corona ($15.5 < {\rm norm_{PL}} < 25.5$) in comparison to those spectral observations where HFQPOs are absent (${\rm norm_{PL}} \sim 30$). Besides this, we notice from Table 2 that the observations with significant HFQPOs have a stronger (${\rm norm_{nth}} \sim 8.0$) and harder ($\Gamma_{\rm nth} \sim 1.73$–$1.79$) 'compact corona' than the observation (Orbit 3841) without an HFQPO. This is an indication that the origin of the HFQPO is due to the oscillations of the 'compact corona' that is represented by the nthComp model. The fact that the powerlaw is strong (${\rm norm_{PL}} \sim 34.9$) and nthComp is comparatively weak (${\rm norm_{nth}} \sim 3.9$) for Orbit 3839 which has the HFQPO with lowest rms (0.83 per cent) also supports our argument that the HFQPO is the result of a compact oscillating corona represented by the nthComp. Dihingia et al. (2019) indicated that HFQPOs at ∼67 Hz in GRS 1915+105 possibly originated due to the quasi-periodic modulation of a very compact inner region of the disc. It is noteworthy that the energy spectra of the source GRO J1655−40 corresponding to the HFQPOs of frequency 300 (Remillard et al. 1999) and 450 Hz (Strohmayer 2001a) possess strong Comptonized contribution extending beyond 100 keV (Aktar et al. 2018). Meanwhile, Remillard et al. (2002) also pointed out that the HFQPOs perhaps originated because of the modulation of the compact Compton corona. Overall, we conjecture that the observed HFQPOs are the manifestation of the oscillations of a 'hot' and compact post-shock corona (Aktar et al. 2018; Dihingia et al. 2019).

In addition, we model the broad-band energy spectra of all the observations using kerrbb model and estimate mass and spin of the source along with the flow accretion rate. Our findings reveal that the mass of the source ($M_{\rm BH}$) lies in the range 12.44–13.09 $M_\odot$ (see Table 3). This estimate is consistent and better constrained compared to the earlier estimates (Greiner et al. 2001; Reid et al. 2014). We find the spin of the source ($a_{\rm k}$) in the range 0.990–0.997 with 90 per cent confidence whereas the previous estimate of spin value was reported as $a_{\rm k} = 0.98 \pm 0.01$ (Shafee et al. 2006; Blum et al. 2009; Miller et al. 2013). The fraction of Compton upscattering ($F_{\rm sca}$) is found to be as high as ∼0.55 when a strong HFQPO is detected (Orbit 3860), whereas $F_{\rm sca}$ is low (0.05) during the absence of HFQPO (Orbit 3841). The index of the simpl convolution model is the lowest (∼3.09) during the non-detection of HFQPO and highest (4.80) during the detection of a strong HFQPO (Orbit 3860). Our results also indicate that the source accretes at super-Eddington rate in the range $1.17 - 1.31\ \dot{M}_{\rm Edd}$ during GT phase of *AstroSat* observations.

In order to improve the error estimation, we have carried out Markov chain Monte Carlo (MCMC) simulations. We use the Goodman–Weare chain algorithm (Goodman & Weare 2010) in XSPEC (Arnaud 1996) with walkers parameter set to 32. The chain length is taken as 15 000 and burn length is fixed to 5000. However, there is no significant improvement in the error estimations. We also cross-check our error estimations using the MCMC hammer algorithm (EMCEE)[7] based on Foreman-Mackey et al. (2013). These results are limited by the unavailability of an analytical approximation for kerrbb model. The results from EMCEE estimation of spin and mass parameters for Orbit 3860 are shown in Fig. 9. The estimate of mass of the BH for this observation is 12.47–13.23 $M_\odot$ and the spin is estimated to be 0.993–0.996 at 90 per cent confidence level. It is to be noted that the errors quoted in this paper are purely statistical and systematics are not accounted for. The top and right-

[7] https://emcee.readthedocs.io/en/stable/#

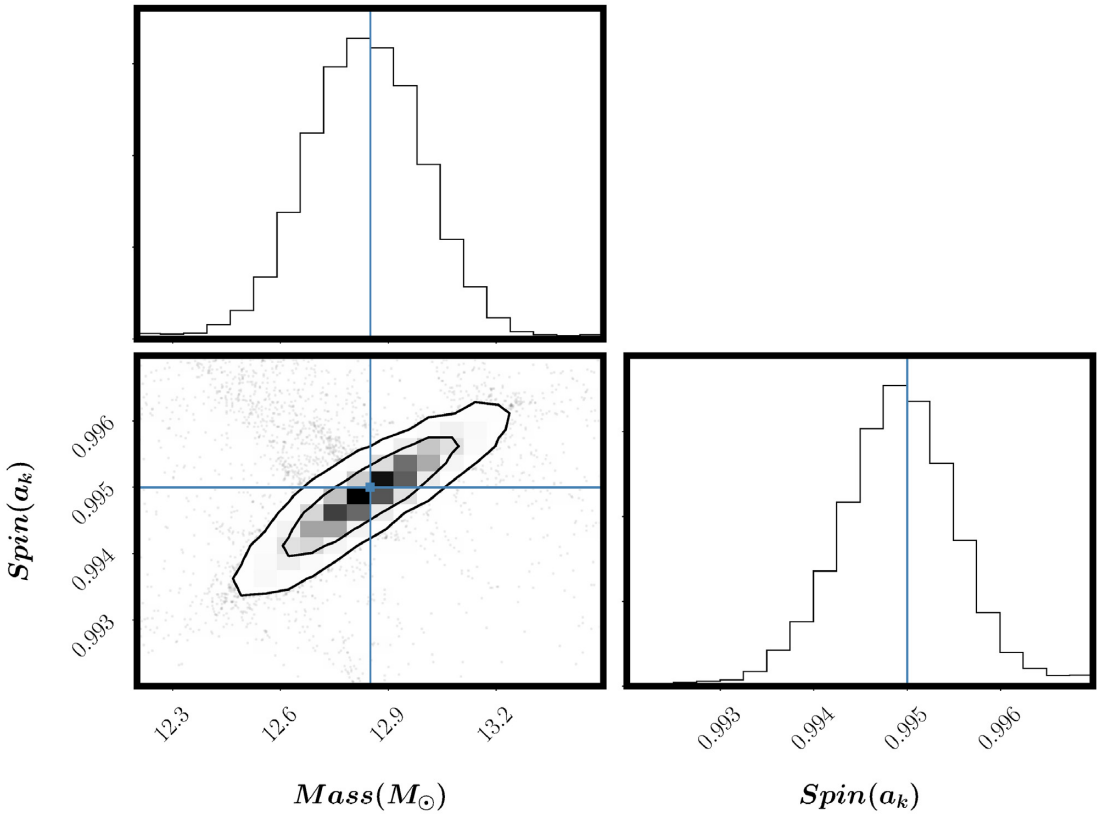

Figure 9. Contour plot of mass versus spin generated using the MCMC Hammer algorithm to determine errors on spin and mass of the BH using data of Orbit 3860. The top panel shows mass distribution and the corner panel shows the contours of mass and spin parameters at 68 per cent and 90 per cent confidence. The right-hand panel shows the spin distribution.

hand panels show mass and spin distribution, respectively, whereas the corner panel shows the confidence contours considering both mass and spin. The contour plot from MCMC simulations and the contour generated from XSPEC (see right-hand panel of Fig. 8) using `steppar` functions are consistent.

Finally, we emphasize that GRS 1915+105 is a maximally rotating, comparatively higher mass X-ray binary source accreting at super-Eddington rate and exhibiting HFQPO features. In addition, we point out that for the first time to the best of our knowledge, the mass, spin, accretion rate, and HFQPOs of GRS 1915+105 are concurrently examined and reported using *AstroSat* observations.

ACKNOWLEDGEMENTS

We thank the anonymous reviewer for his/her suggestions and comments that helped us to improve the quality of this manuscript. AN, VKA, and MCR thank DD, PDMSA and Director, URSC for encouragement and continuous support to carry out this research. HS thanks Department of Physics, IIT Guwahati for providing the facilities to complete part of this work. This research made use of the data obtained through GT phase of *AstroSat* observations. The authors thank the SXT-POC of TIFR and the *LAXPC* team of IUCAA and TIFR for providing the data extraction software for the respective instruments.

DATA AVAILABILITY

Data used for this publication are currently available at the Astrobrowse (AstroSat archive) website (https://astrobrowse.issdc.gov.in/astro_archive/archive) of the Indian Space Science Data Center (ISSDC).

REFERENCES

Agrawal P. C. et al., 2017, J. Astrophys. Astron., 38, 30
Agrawal V. K., Nandi A., Girish V., Ramadevi M. C., 2018, MNRAS, 477, 5437
Aktar R., Das S., Nandi A., Sreehari H., 2018, J. Astrophys. Astron., 39, 17
Alam M. S., Dewangan G. C., Belloni T., Mukherjee D., Jhingan S., 2014, MNRAS, 445, 4259
Altamirano D., Belloni T., 2012, ApJ, 747, L4
Antia H. M. et al., 2017, ApJS, 231, 10
Arnaud K. A., 1996, in Jacoby G. H., Barnes J., eds, ASP Conf. Ser. Vol. 101, Astronomical Data Analysis Software and Systems V. Astron. Soc. Pac., San Francisco, p. 17
Bachetti M. et al., 2015, ApJ, 800, 109
Belloni T. M., Altamirano D., 2013, MNRAS, 432, 10
Belloni T. M., Motta S. E., 2016, in Bambi C., ed., Astrophysics and Space Science Library, Vol. 440, Astrophysics of Black Holes: From Fundamental Aspects to Latest Developments. Springer-Verlag, Berlin, p. 61
Belloni T., Klein-Wolt M., Méndez M., van der Klis M., van Paradijs J., 2000, A&A, 355, 271
Belloni T., Méndez M., Sánchez-Fernández C., 2001, A&A, 372, 551
Belloni T., Homan J., Casella P., van der Klis M., Nespoli E., Lewin W. H. G., Miller J. M., Méndez M., 2005, A&A, 440, 207
Belloni T., Soleri P., Casella P., Méndez M., Migliari S., 2006, MNRAS, 369, 305
Belloni T. M., Bhattacharya D., Caccese P., Bhalerao V., Vadawale S., Yadav J. S., 2019, MNRAS, 489, 1037

Blum J. L., Miller J. M., Fabian A. C., Miller M. C., Homan J., van der Klis M., Cackett E. M., Reis R. C., 2009, ApJ, 706, 60
Castro-Tirado A. J., Brandt S., Lund N., 1992, in Green D. W. E., ed, Proc. IAU Circ. 5590, International Astronomical Union Circulars
Chakrabarti S., Titarchuk L. G., 1995, ApJ, 455, 623
Cui W., 1999, ApJ, 524, L59
Cui W., 2000, ApJ, 534, L31
Cui W., Zhang S. N., Chen W., 1998, ApJ, 492, L53
Dihingia I. K., Das S., Maity D., Nand i A., 2019, MNRAS, 488, 2412
Done C., Wardziński G., Gierliński M., 2004, MNRAS, 349, 393
Ebisawa K., Życki P., Kubota A., Mizuno T., Watarai K.-Y., 2003, ApJ, 597, 780
Fender R. P., Homan J., Belloni T. M., 2009, MNRAS, 396, 1370
Feroci M., Matt G., Pooley G., Costa E., Tavani M., Belloni T., 1999, A&A, 351, 985
Foreman-Mackey D., Hogg D. W., Lang D., Goodman J., 2013, PASP, 125, 306
García J. et al., 2014, ApJ, 782, 76
Goodman J., Weare J., 2010, Commun. Appl. Math. Comput. Sci., 5, 65
Greiner J., Cuby J. G., McCaughrean M. J., 2001, Nature, 414, 522
Grove J. E., Johnson W. N., Kroeger R. A., McNaron-Brown K., Skibo J. G., Phlips B. F., 1998, ApJ, 500, 899
Hannikainen D. C. et al., 2005, A&A, 435, 995
Iyer N., Nandi A., Mandal S., 2015, ApJ, 807, 108
Klein-Wolt M., Fender R. P., Pooley G. G., Belloni T., Migliari S., Morgan E. H., van der Klis M., 2002, MNRAS, 331, 745
Leahy D. A., Chen Y., 2019, ApJ, 871, 152
Leahy D. A., Darbro W., Elsner R. F., Weisskopf M. C., Sutherland P. G., Kahn S., Grindlay J. E., 1983, ApJ, 266, 160
Li L.-X., Zimmerman E. R., Narayan R., McClintock J. E., 2005, ApJS, 157, 335
Méndez M., Altamirano D., Belloni T., Sanna A., 2013, MNRAS, 435, 2132
Merloni A., Vietri M., Stella L., Bini D., 1999, MNRAS, 304, 155
Miller J. M. et al., 2013, ApJ, 775, L45
Morgan E. H., Remillard R. A., Greiner J., 1997, ApJ, 482, 993
Nandi A., Debnath D., Mandal S., Chakrabarti S. K., 2012, A&A, 542, A56
Nandi A., Radhika D., Seetha S., 2013, in Santabrata D., Anuj N., Indranil C., eds, Astronomical Society of India Conference Series, Astronomical Society of India, p. 71
Nowak M. A., Wagoner R. V., Begelman M. C., Lehr D. E., 1997, ApJ, 477, L91
Punsly B., Rodriguez J., 2013, ApJ, 764, 173
Radhika D., Nandi A., 2014, Adv. Space Res., 54, 1678
Radhika D., Nandi A., Agrawal V. K., Seetha S., 2016, MNRAS, 460, 4403
Radhika D., Sreehari H., Nandi A., Iyer N., Mand al S., 2018, Ap&SS, 363, 189
Ratti E. M., Belloni T. M., Motta S. E., 2012, MNRAS, 423, 694
Rebusco P., 2008, New A Rev., 51, 855
Reid M. J., McClintock J. E., Steiner J. F., Steeghs D., Remillard R. A., Dhawan V., Narayan R., 2014, ApJ, 796, 2
Remillard R. A., McClintock J. E., 2006, ARA&A, 44, 49
Remillard R. A., Morgan E. H., McClintock J. E., Bailyn C. D., Orosz J. A., 1999, ApJ, 522, 397
Remillard R. A., Muno M. P., McClintock J. E., Orosz J. A., 2002, ApJ, 580, 1030
Rezzolla L., Yoshida S., Maccarone T. J., Zanotti O., 2003, MNRAS, 344, L37
Seward F. D., Charles P. A., 2010, Exploring the X-ray Universe. Cambridge Univ. Press, Cambridge
Shafee R., McClintock J. E., Narayan R., Remillard R. A., Davis S. W., Li L., 2006, BAAS, 38, 343
Shakura N. I., Sunyaev R. A., 1973, A&A, 24, 337
Singh K. P., Stewart G. C., Westergaard N. J., Bhattacharayya S., Chandra S. et al., 2017, J. Astrophys. Astron., 38, 29
Sreehari H., Ravishankar B. T., Iyer N., Agrawal V. K., Katoch T. B., Mandal S., Nand i A., 2019, MNRAS, 487, 928
Stefanov I. Z., 2014, MNRAS, 444, 2178
Steiner J. F., Narayan R., McClintock J. E., Ebisawa K., 2009, PASP, 121, 1279
Stella L., Vietri M., 1998, ApJ, 492, L59
Strohmayer T. E., 2001a, ApJ, 552, L49
Strohmayer T. E., 2001b, ApJ, 554, L169
Sunyaev R. A., Titarchuk L. G., 1980, A&A, 86, 121
Tanaka Y., Lewin W. H. G., 1995, X-ray Binaries, Cambridge University Press, Cambridge, U.K., p. 126
van der Klis M., 1988, in Ögelman H., van den Heuvel E. P. J., eds, NATO Advanced Science Institutes (ASI) Series C Vol. 262. Kluwer Academic Publishers, Dordrecht, p. 27
van der Klis M., Jansen F., van Paradijs J., Lewin W. H. G., van den Heuvel E. P. J., Trumper J. E., Szatjno M., 1985, Nature, 316, 225
Varniere P., Vincent F. H., Casse F., 2020, A&A, 638, A33
Vilhu O., Poutanen J., Nikula P., Nevalainen J., 2001, ApJ, 553, L51
Vincent F. H., Meheut H., Varniere P., Paumard T., 2013, A&A, 551, A54
Yadav J. S. et al., 2016, ApJ, 833, 27
Zdziarski A. A., 2014, MNRAS, 444, 1113
Zdziarski A. A., Johnson W. N., Magdziarz P., 1996, MNRAS, 283, 193
Zdziarski A. A., Grove J. E., Poutanen J., Rao A. R., Vadawale S. V., 2001, ApJ, 554, L45
Zhang W., Jahoda K., Swank J. H., Morgan E. H., Giles A. B., 1995, ApJ, 449, 930

This paper has been typeset from a TEX/LATEX file prepared by the author.